ARTICLE OPEN

Check for updates

Revealing inherent quantum interference and entanglement of a Dirac particle

Wen Ning[1,4], Ri-Hua Zheng[1,4], Yan Xia[1], Kai Xu[2,3], Hekang Li[2], Dongning Zheng[2,3], Heng Fan[2,3], Fan Wu[1✉], Zhen-Biao Yang[1✉] and Shi-Biao Zheng[1✉]

Although originally predicted in relativistic quantum mechanics, *Zitterbewegung* can also appear in some classical systems, which leads to the important question of whether *Zitterbewegung* of Dirac particles is underlain by a more fundamental and universal interference behavior without classical analogs. We here reveal such an interference pattern in phase space, which underlies but goes beyond *Zitterbewegung*, and whose nonclassicality is manifested by the negativity of the phase space quasiprobability distribution, and the associated pseudospin-momentum entanglement. We confirm this discovery by numerical simulation and an on-chip experiment, where a superconducting qubit and a quantized microwave field respectively emulate the internal and external degrees of freedom of a Dirac particle. The measured quasiprobability negativities agree well with the numerical simulation. Besides being of fundamental importance, the demonstrated nonclassical effects are useful in quantum technology.

npj Quantum Information (2023)9:99 ; https://doi.org/10.1038/s41534-023-00770-0

INTRODUCTION

The Dirac equation, which describes the wavefunction for a spin-1/2 particle in the framework of relativistic quantum mechanics, represents a cornerstone of modern physics. Over the past century, this equation has been producing enduring profound influences on a wide variety of fields of modern science and technology, ranging from atomic physics to quantum electrodynamics[1], and from material engineering[2–5] to medical imaging[6].

Despite the fundamental importance of the Dirac equation, the physics underlying its dynamical solution has not been fully understood owing to the associated elusive phenomena, exemplified by *Zitterbewegung* (*ZB*)[7], the oscillatory motion of a particle, as a result of the interference between the positive and negative energy components. For a free electron, the predicted *ZB* has an amplitude on the order of the Compton wavelength, $\hbar/mc \sim 10^{-12}$ m, and thus cannot be unambiguously observed due to the restriction of the Heisenberg uncertainty principle. Although whether or not *ZB* really exists in relativistic quantum mechanics is still an open question[8–11], enduring efforts have been made to its simulations with different quantum systems, including circuit quantum electrodynamics[11], ion traps[12,13], ultracold atoms[14–17], semiconductor quantum wells[18–23], graphene[24–33], and moiré excitons[34]. These investigations have shed new light on *ZB*, which itself, however, is not a unique character of Dirac particles as similar phenomena can also appear in some classical wave systems[35–40]. This leads us to consider whether the *ZB* associated with Dirac particles has a deeper quantum origin that can manifest itself even without *ZB*. Answering this question is critical for understanding the dynamical behaviors of Dirac particles at a more fundamental level, but a deep exploration is still lacking.

RESULTS

Theoretical predictions

We here present an investigation on this important issue, and unveil a universal quantum interference behavior in the position-momentum space. The nonclassicality of this behavior is manifested by the negativity of the phase space quasiprobability distribution–Wigner function (WF), as well as by the quantum correlation between the spatial and internal degrees of freedom. These quantum signatures distinguish the *ZB* of the Dirac particle, obtained by integrating the WF over the momentum, from the trembling motion of classical wavepackets, and more importantly, can express themselves even in the absence of any negative component. We demonstrate this unique interference pattern with a circuit, where the spinorial characteristic of a Dirac particle is encoded in the two lowest energy levels of a superconducting Xmon qubit[41–43], while the position and momentum are mapped to the quadratures of the photonic field. The measured WFs and entanglement entropy agree well with theoretical predictions. Furthermore, we simulate the Klein tunneling[44,45] in a linear potential field and observe mesoscopic superpositions of two separated wavepackets in phase space.

We focus on the simplest case that the motion of a Dirac particle is confined to one dimension (1D), for which the Hamiltonian reduces to

$$H_D = c\sigma_y\hat{p} + mc^2\sigma_z. \quad (1)$$

Here c denotes the light speed in the vacuum, $\hat{p}$ represents the momentum operator of the particle with a rest mass of m, and σ_y and σ_z are the Pauli operators that endow the Dirac particle a spinor characteristic, manifested by a two-component wavefunction, where the spatial position and momentum are correlated with the degree of freedom defined in an "internal space", which will be referred to as pseudospin for simplicity. Unlike the

[1]Fujian Key Laboratory of Quantum Information and Quantum Optics, College of Physics and Information Engineering, Fuzhou University, Fuzhou, Fujian 350108, China. [2]Institute of Physics, Chinese Academy of Sciences, Beijing 100190, China. [3]CAS Center for Excellence in Topological Quantum Computation, University of Chinese Academy of Sciences, Beijing 100190, China. [4]These authors contributed equally: Wen Ning, Ri-Hua Zheng ✉email: t21060@fzu.edu.cn; zbyang@fzu.edu.cn; t96034@fzu.edu.cn

Schrödinger equation, the Dirac equation is linear in both the time- and space-derivatives, satisfying the Lorentz-covariance, and includes the spin degree of freedom at the ab initio level by describing the wave function in terms of a spinor. These features have led to remarkable accomplishments, including predictions of the spin-1/2 feature of electrons and the existence of anti-particles indicated by the negative-energy component accompanying the positive one, and introduction of the spin-orbit interaction that led to a more refined fine structure description of the spectrum. These predictions are based on stationary solutions of the Dirac equation and show excellent agreements with experiments. As the Hamiltonian commutes with the momentum operator, it is illuminating to uncover the physics in the momentum representation, where the momentum operator $\hat{p}$ can be taken as a parameter p. For a specific value of p, $H_{\rm D}$ has two eigenvalues $\pm E_p = \pm\sqrt{p^2c^2 + m^2c^4}$, with the corresponding eigenstates $|\phi_+(p)\rangle = (\cos\phi_p, \mathrm{i}\sin\phi_p)^T$ and $|\phi_-(p)\rangle = (\mathrm{i}\sin\phi_p, \cos\phi_p)^T$, where $\tan(2\phi_p) = \frac{p}{mc}$. Suppose that the system is initially in the product state

$$|\psi(0)\rangle = \int \mathrm{d}p\, \xi_p |p\rangle |X\rangle, \tag{2}$$

where $|\pm X\rangle = \frac{1}{\sqrt{2}}(1, \pm 1)^T$ and ξ_p denotes the wave function in the momentum representation. Under the Dirac Hamiltonian, the system evolves as

$$|\psi(t)\rangle = \int \mathrm{d}p\, |p\rangle \xi_p (\cos\varphi_t |X\rangle - \mathrm{i}\mathrm{e}^{-2\mathrm{i}\phi_p}\sin\varphi_t |-X\rangle), \tag{3}$$

where $\varphi_t = E_p t/\hbar$. This directly yields the average position evolution,

$$\begin{aligned}\langle x(t)\rangle &= \langle x(0)\rangle + \langle v(0)\rangle t \\ &\quad + \hbar\int \mathrm{d}p\, |\xi_p|^2 x_p(1-\cos 2\varphi_t),\end{aligned} \tag{4}$$

where $x_p = \mathrm{d}\phi_p/\mathrm{d}p$, $\langle x(0)\rangle$ represents the average value of the initial position, and $\langle v(0)\rangle$ denotes the initial mean velocity. The *ZB*, manifested by the last term, is observable only in the intermediate regime where mc is comparable with p.

In the non-relativistic regime $|p| \ll mc$, the *ZB* amplitude $A \simeq \lambda_c/2$, where $\lambda_c = \hbar/mc$ is the Compton wavelength, which sets the lower bound for the uncertainty of the position, and consequently, the *ZB* cannot be observed. In the far-relativistic regime $|p| \gg mc$, $A \ll \hbar/2\langle p\rangle \ll \delta x$, where $\delta x = \hbar/2\delta p$ is the limitation of precision attainable for any position measurement imposed by the Heisenberg uncertainty relation.

As we have noted, *ZB* itself does not manifest quantum effects, but is closely related to quantum entanglement between the internal and spatial degrees of freedom, produced by their coupling. Under the time evolution, the populations of two states $|\pm X\rangle$ become increasingly balanced, and the entropy tends to 1. Due to this entanglement, the spatial quantum interference appears when the WF is correlated with the projection of the pseudospin along some basis, e.g., $\{|\pm B\rangle\}$. The WFs associated to $|\pm B\rangle$ are respectively

$$\mathcal{W}_\pm(x,p) = \frac{1}{\pi\hbar}\int \mathrm{d}v\, \phi_\pm^*(p+v)\phi_\pm(p-v)\mathrm{e}^{-2\mathrm{i}vx/\hbar}, \tag{5}$$

where $\phi_\pm(p) = \xi_p\langle \pm B|(\cos\varphi_t|X\rangle - \mathrm{i}\mathrm{e}^{-2\mathrm{i}\phi_p}\sin\varphi_t|-X\rangle)$. During the evolution, the wavepacket is continually deformed under the competition between the momentum-dependent and static energy terms in the Dirac Hamiltonian, which leads to a nonlinear dependence of the energy on the momentum. This nonlinear process evolves an initial Gaussian wavepacket to a non-Gaussian one, manifesting pseudospin-dependent quantum interference signatures. The *ZB* phenomenon appears as the integral of the weighted mixture of the two WFs over the momentum, which reflects the classical probability distribution, but does not manifest the underlying quantum nature. It should be noted that the presence of *ZB* is challenged by the claim that the positive and negative components could not be assigned to a single particle[8], however, recent experimental evidence indicates nature does not prohibit the existence of a quantum superposition of a particle with its antiparticle[46]. We further note that even when the particle remains in the positive branch, there still exists phase space quantum interference, though *ZB* disappears.

Device and experimental scheme

The simulation is performed with a superconducting qubit of angular frequency ω_0 that encodes the internal state of the simulated spinor, whose position and momentum are mapped onto the two quadratures of the microwave field stored in a bus resonator, defined as $\hat{x} = \frac{1}{\sqrt{2}}(a^\dagger + a)$ and $\hat{p} = \frac{\mathrm{i}}{\sqrt{2}}(a^\dagger - a)$, where $a^\dagger$ and a denote the creation and annihilation operators for the photonic field of angular frequency ω_r. If we take $\hbar = 1$, $\hat{x}$ and $\hat{p}$ satisfy the same commutation relation as the position and momentum operators. The qubit is subjected to two longitudinal parametric modulations with amplitudes ε_j and angular frequencies ν_j ($j = 1, 2$), and a transverse continuous microwave driving with an amplitude Ω (Fig. 1a). With the choice $\omega_r = \omega_0 + 2\nu_1$, the resonator is coupled to the qubit at the second upper sideband of the first modulation with the effective strength $\eta = \lambda J_2(\mu)/2$[47], where $J_n(\mu)$ is the nth Bessel function of the first kind, with $\mu = \varepsilon_1/\nu_1$. When $\Omega \gg 2\eta$, the transverse drive effectively transforms the rotating-wave interaction into an equal combination of rotating- and counter-rotating-wave interactions, simulating the coupling between the internal and external degrees of freedom of the spinor. Then the resulting effective Hamiltonian reduces to the form of Eq. (1), with the correspondences $\sigma_y = \mathrm{i}|g\rangle\langle e| - \mathrm{i}|e\rangle\langle g|$, $\sigma_z = |e\rangle\langle e| - |g\rangle\langle g|$, $c^* = \sqrt{2}\eta$ and $m^*c^{*2} = \varepsilon_2/4$, where c^* and m^* denote the effective light speed and mass of the Dirac particle in the simulation, respectively (see Supplementary Note 1).

Before the experiment, both the resonator and the spinor qubit are initialized to their ground states. The experiment starts with the application of a pulse to the resonator, translating its state along the p-axis in phase space by an amount of $p_0 = 2$, and thus transforming the initial vacuum state to the coherent state $|\mathrm{i}\sqrt{2}\rangle$. Then a $\pi/2$ rotation is performed on the test qubit, transforming it from $|g\rangle$ to $|X\rangle$ at the operating frequency $\omega_0/(2\pi) = 5.26$ GHz. The initial qubit-resonator state is pictorially shown in Fig. 1b. After this initial state preparation, two parametric modulations with frequencies $\nu_1/(2\pi) = 160$ MHz and $\nu_2/(2\pi) = 33.4$ MHz are applied to the qubit. These modulations, together with the transverse microwave driving at the frequency ω_0, couple the qubit to the bus resonator with a fixed frequency of $\omega_r/(2\pi) = 5.584$ GHz, effectively realizing the Dirac Hamiltonian in the rotating frame. The ratio between the effective momentum and mass of the Dirac particle is controlled by adjusting the modulation amplitudes ε_1 and/or ε_2. Detailed system parameters are shown in the Supplementary Table 1.

ZB interference behaviors

We investigate the interference behaviors with the choice of effective spinor frequency $\omega = m^*c^* = \sqrt{2}\eta p_0$, with $c^* = \sqrt{2}\eta$, which ensures that the Dirac particle described by the Dirac equation $H_{\rm D}$ has an initial momentum of p_0. After a preset evolution time, both the parametric modulations and microwave driving are switched off. This is followed by Wigner tomography, realized by performing a phase space displacement, $D(\gamma) = \mathrm{e}^{\gamma a^\dagger - \gamma^* a}$, to the resonator and then tuning an ancilla qubit on resonance with the resonator. The photon number population of the displaced resonator field, $\mathcal{P}_n(\gamma)$, inferred from the measured Rabi oscillation signals, directly yields the WF, $\mathcal{W}(x,p) = \frac{1}{\pi}\sum_n(-1)^n\mathcal{P}_n(\gamma)$[47,48], where $x = \sqrt{2}\mathrm{Re}\gamma$ and $p = \sqrt{2}\mathrm{Im}\gamma$. The nonclassical features of the simulated Dirac

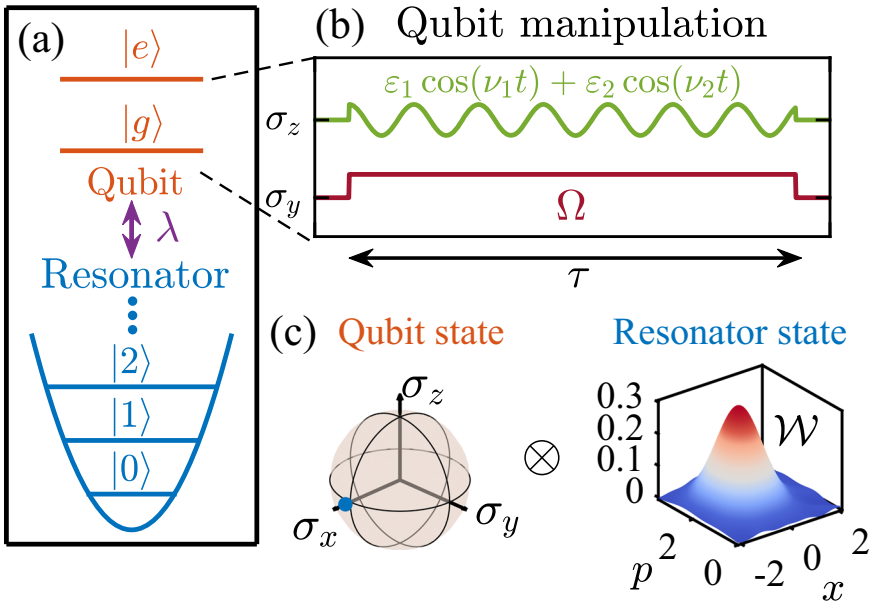

Fig. 1 Diagram and pulse for simulating 1D Dirac particles. a Analog of the Dirac particle in a circuit. The internal and external degrees of freedom of the Dirac particle are respectively encoded in a superconducting qubit and the field mode in a microwave resonator, whose quadratures behave like the position (x) and momentum (p) of the particle. **b** Engineering of the Dirac Hamiltonian. The coupling between the internal and external states of the spinor is simulated by transversely driving the qubit with continuous microwave, and longitudinally modulating it with two alternating current (AC) fluxes. The first parametric modulation controls the qubit-resonator interaction at the second upper sideband, which together with the transverse driving, effectively realizes the momentum term. The second parametric modulation serves for adjusting the effective mass of the simulated particle. **c** Pictorial representation of the system's initial state. The qubit's state $|X\rangle$ is represented by its Bloch vector, while the resonator's coherent state $|\mathrm{i}\sqrt{2}\rangle$ is characterized by its WF.

particle can be revealed by the WFs of the resonator conditional on the detection of the qubit state. The WFs correlated with the measurement outcomes $|g\rangle$ and $|e\rangle$ are presented in the upper panels of Fig. 2a, b, and the result irrespective of the test qubit's state is displayed in Fig. 2c, all measured after an evolution time 330 ns. As expected, during the evolution the initial Gaussian wavepacket is split into two parts, propagating towards opposite directions. The WF associated with each qubit state displays a region of negativity that is a purely quantum-mechanical effect. This result can be interpreted as follows. Under the Dirac Hamiltonian, each component accumulates a phase that non-linearly depends on the "momentum" and "mass" as $\sqrt{p^2+(m^*c^*)^2}c^*t$. Such a process corresponds to a non-Gaussian operation, turning a Gaussian state to a non-Gaussian state. The two rods sprouting from the bulk of the distorted wavepacket interfere with each other, resulting in a negative quasiprobability distribution in the region between them. The lower panels show the probability distribution $\mathcal{P}(x)$ with respect to the quadrature x, obtained by integrating $\mathcal{W}(x,p)$ over p.

Another important feature associated with the simulated particle is the production of quantum entanglement between its internal and external degrees of freedom. To quantitatively characterize the behavior, we present the von Neumann entropy of the test qubit, $\mathcal{S}=-\mathrm{tr}(\rho_q\log_2\rho_q)$, measured for different evolution time t in Fig. 2d, where ρ_q denotes the reduced density operator of this qubit. The measured results (red circles) agree with the numerical simulation (blue curve), where the small fluctuations are due to the fast Rabi oscillations. *ZB* is manifested in the time-evolving mean position, which is related to $\mathcal{P}(x)$ by $\langle x\rangle=\mathrm{tr}(\rho x)$, where ρ is the corresponding density matrix deduced by the measured WF data (see Supplementary Note 5). This evolution, inferred from the measured WF, is presented in Fig. 2e, which coincides with the simulation (green curve), confirming that *ZB* has a deeper root that is of pure quantum characteristic. We notice that the numerical simulation curves of Fig. 2d, e both have high frequency vibrations. The high-frequency signals mainly come from the first parametric modulation with frequency $2\pi\times160$ MHz, whose Jacobi-Anger expansion will produce two major frequency components of $2\pi\times160$ MHz and $2\pi\times320$ MHz around the dynamically resonant frequency (see Supplementary Note 1).

Although *ZB* appears only when the system is in a superposition of positive and negative components, phase space quantum interference is actually a universal inherent characteristic of Dirac particles, which can manifest itself even without negative components. This point can be illustrated with the representative example, where the momentum has a Gaussian distribution, centered at p_0 with the spread δp. When restricted to the positive branch, the system state can be written as

$$|\psi(t)\rangle=\int \mathrm{d}p\,\mathrm{e}^{\mathrm{i}\theta_p(t)}\xi_p|p\rangle|\phi_+(p)\rangle, \tag{6}$$

where $\xi_p=(\delta p\sqrt{2\pi})^{-1/2}\mathrm{e}^{-(p-p_0)^2/(2\delta p)^2}$. This implies that the internal degrees freedom is necessarily entangled with the momentum except for a plane wave with $\delta p\to0$. As it is experimentally difficult to prepare such an entangled state, we reveal the associated quantum feature by numerical simulation. The entanglement entropy as a function of δ_p is shown in Fig. 3a, which is independent of the evolution time. We here have set $\hbar=c=1$ and $m=p_0=1$. Unlike the entropy, the phase space interference pattern is time-dependent. To clearly reveal such an interference behavior, we assume that $\delta p=1$, and $\theta_p(0)=0$. The unconditional WFs, for different evolution times under the ideal Dirac Hamiltonian, are shown in Fig. 3b. Unexpectedly, the WF displays a time-evolving quantum interference pattern, even without correlating the result with the internal state. We note that the phase space quantum interference effects were previously predicted for some special states with both positive and negative components[11], but the presence of such effects without *ZB* has not been revealed. The WFs correlated with $|g\rangle$ and $|e\rangle$, together

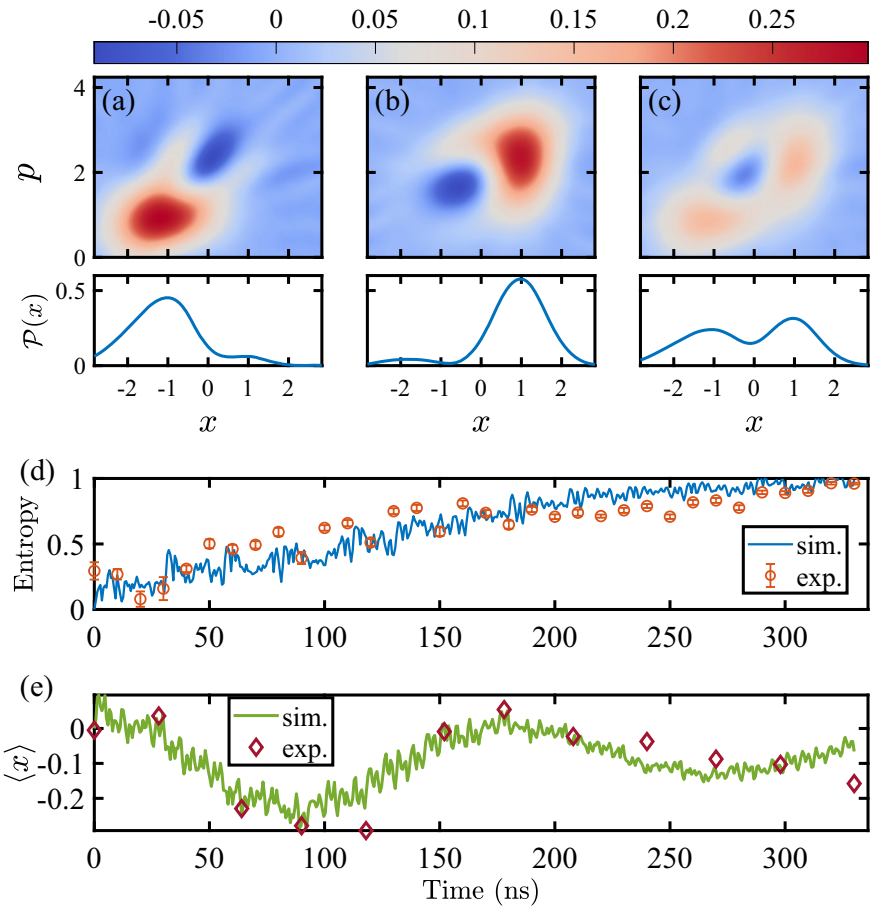

Fig. 2 Observation of phase space quantum interference. WFs correlated with the basis states $|g\rangle$ (**a**) and $|e\rangle$ (**b**) of the test qubit; (**c**) WF irrespective of the test qubit's state, all measured after an evolution time of 330 ns. Probability distributions $\mathcal{P}(x)$ with respect to the quadrature x, shown in the lower panels, are obtained by integrating the WF $\mathcal{W}(x,p)$ over p. **d** Entropy evolution of the test qubit. This entropy is directly obtained from the density matrix of the qubit, measured irrespective of the resonator's state. Symbols "exp." and "sim." represent the experimental and corresponding simulated data, respectively. **e** Evolution of the average value of the resonator's quadrature $\langle x \rangle$. The value at each point is extracted from the measured WF.

with the evolutions of mean position and entanglement entropy, are displayed in the Supplementary Note 3.

Klein tunneling

Pushing one step further, we simulate Klein tunneling in a linear potential field[40,44]. It was first noted by Klein that a relativistic electron may exhibit a counter-intuitive behavior when confronted with a semi-infinite step potential with $V = 0$ and V_0 for $x < 0$ and $x \geq 0$, respectively. This occurs in the regime $V_0 > E + mc^2$, for which the electron can propagate through the barrier without damping, where it is transformed into a positron, where E denotes the initial kinetic energy. In our setup, it is not easy to engineer the step-shaped potential. However, a linear potential can be added to the Dirac Hamiltonian in situ by applying a continuous microwave to the resonator, given by $V = \sqrt{2}\epsilon x$, where ϵ is the amplitude of the drive, and set to be $2\pi \times 0.39$ MHz in our experiment. For simplicity, the simulation is performed for the choice $\varepsilon_2 = 0$. Figure 4a, b showcase the WFs of the resonator correlated with the states $|g\rangle$ and $|e\rangle$ of the spinor qubit, respectively, and Fig. 4c presents the result irrespective of the qubit's state, all measured after an evolving time $t = 288$ ns. As expected, the linear potential drags the phase space evolution down along the p-axis by an amount $\sqrt{2}\epsilon t$, but does not affect the motion along the x-axis. The resulting cat-like state was previously predicted to exist as a solution of a relativistic spin-1/2 charged particle in an external magnetic field[49], but has not been characterized in previous simulations[50,51]. To illustrate this phenomenon more clearly, we display the time evolutions of the measured $\langle x \rangle$ and $\langle p \rangle$ in Fig. 4d, e, respectively, where the dots and diamonds respectively denote the results for wavepackets along the positive and negative directions of the x-axis. The measured results imply that the two wavepackets have the same momentum at each moment, but move along the opposite directions. This can be explained as follows. For $x > 0$, the momentum of the Dirac particle is given by $p^2 = (E - V)^2 - m^2$ ($c = 1$), with the group velocity $v_g = dE/dp = p/(E - V)$[45]. When the massless particle moves from left to right with $E < V$, p is assigned with its negative solution, so that v_g is positive.

DISCUSSION

We have performed an investigation on the dynamical evolution of the Dirac particle, showing that the competition between its dynamic and static energies leads to a time-evolving phase space quasi-probability distribution, which underlies its spatial motion. The quantum interference signatures appear in the phase space spanned by position and momentum, but disappear when the momentum is traced out. We demonstrate this discovery with numerical simulations and with a circuit experiment, where a superconducting qubit represents the

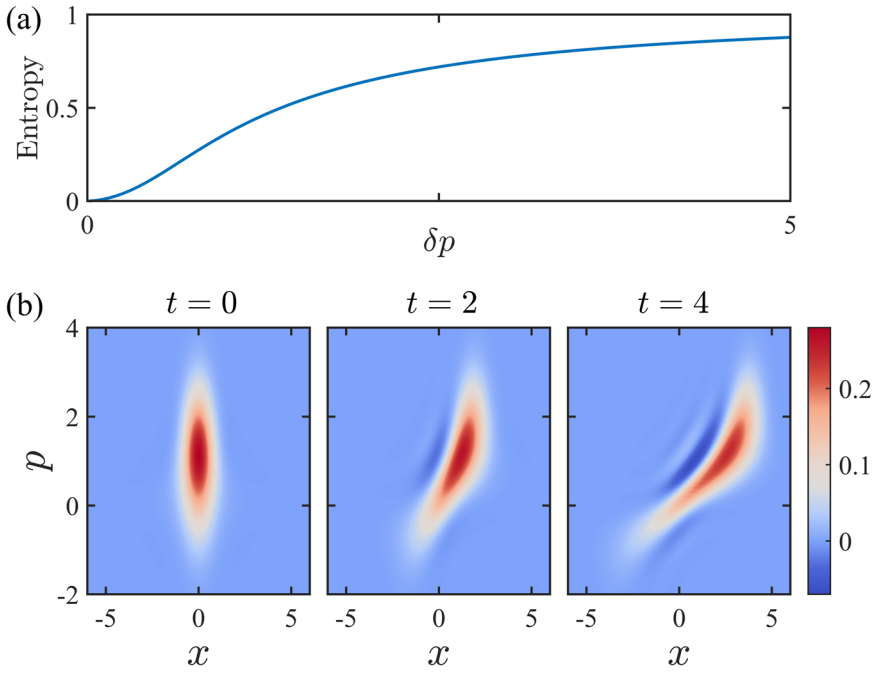

Fig. 3 Quantum characteristics in the positive branch. a Entanglement entropy versus the momentum spread. **b** WF evolution with a momentum spread $\delta p = 1$. In the numerical simulations, the Dirac particle is supposed to have a mass of $m = 1$ and a Gaussian momentum distribution with a mean value of $p_0 = 1$. For simplicity, we here take the natural unit with $\hbar = c = 1$.

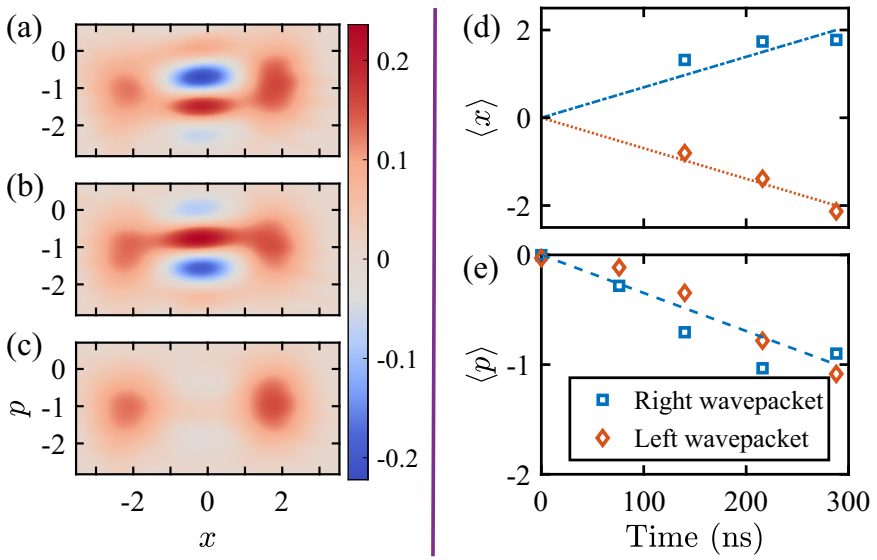

Fig. 4 Simulation of Klein's tunneling. The potential is simulated by applying a drive to the resonator with the strength $\epsilon = 2\pi \times 0.39$ MHz. The simulation is performed without the second parametric modulation so that the system dynamics are analogous to a massless particle penetrating a linear potential. **a** Measured WF of the resonator conditional on the detection of the spinorial state $|g\rangle$. **b** Resonator's WF correlated with the detection of $|e\rangle$. **c** Unconditional WF. These WFs are reconstructed for the system evolving from the initial ground state $|g, 0\rangle$ for a time 288 ns. **d**, **e** Evolutions of the measured $\langle x \rangle$ and $\langle p \rangle$. The dots and diamonds denote the measured values for wavepackets along the positive and negative directions of the x-axis, and the triangles correspond to the results without discrimination between the moving directions.

internal degree of freedom, which is coupled to the microwave field in a resonator that encodes the spatial degree of freedom. The measured negativities of the WFs and entanglement entropy distinguish the *ZB* of the Dirac particle from that exhibited by the classical systems. In addition to fundamental interest, the demonstrated nonclassicality can serve as a resource for quantum-enhanced sensing[52].

DATA AVAILABILITY

All data needed to evaluate the conclusions in the paper are present in the paper and the Supplementary Materials. Additional data related to this paper may be requested from the authors.

Received: 4 May 2023; Accepted: 26 September 2023;
Published online: 10 October 2023

REFERENCES

1. Thaller, B. *The Dirac Equation*. (Springer Berlin Heidelberg, Berlin, Heidelberg, 1992).
2. Castro Neto, A. H., Guinea, F., Peres, N. M. R., Novoselov, K. S. & Geim, A. K. The electronic properties of graphene. *Rev. Mod. Phys.* **81**, 109 (2009).
3. Novoselov, K. S. et al. Two-dimensional gas of massless Dirac fermions in graphene. *Nature* **438**, 197 (2005).
4. Park, C.-H., Yang, L., Son, Y.-W., Cohen, M. L. & Louie, S. G. Anisotropic behaviours of massless Dirac fermions in graphene under periodic potentials. *Nat. Phys.* **4**, 213 (2008).
5. Tarruell, L., Greif, D., Uehlinger, T., Jotzu, G. & Esslinger, T. Creating, moving and merging Dirac points with a Fermi gas in a tunable honeycomb lattice. *Nature* **483**, 302 (2012).
6. Beyer, T. et al. A combined PET/CT scanner for clinical oncology. *J. Nucl. Med.* **41**, 1369 (2000).
7. Schrödinger, E. Über die kräftefreie bewegung in der relativistischen quantenmechanik. *Sitz. Preuss. Akad. Wiss. Phys.-Math. Kl.* **24**, 418 (1930).
8. Foldy, L. L. & Wouthuysen, S. A. On the Dirac theory of spin 1/2 particles and its non-relativistic limit. *Phys. Rev.* **78**, 29 (1950).
9. Krekora, P., Su, Q. & Grobe, R. Relativistic electron localization and the lack of *Zitterbewegung*. *Phys. Rev. Lett.* **93**, 043004 (2004).
10. Wang, Z.-Y. & Xiong, C.-D. *Zitterbewegung* by quantum field-theory considerations. *Phys. Rev. A* **77**, 045402 (2008).
11. Pedernales, J. S., Di Candia, R., Ballester, D. & Solano, E. Quantum simulations of relativistic quantum physics in circuit QED. *New J. Phys.* **15**, 055008 (2013).
12. Lamata, L., León, J., Schätz, T. & Solano, E. Dirac equation and quantum relativistic effects in a single trapped ion. *Phys. Rev. Lett.* **98**, 253005 (2007).
13. Gerritsma, R. et al. Quantum simulation of the Dirac equation. *Nature* **463**, 68 (2010).
14. Vaishnav, J. Y. & Clark, C. W. Observing *Zitterbewegung* with ultracold atoms. *Phys. Rev. Lett.* **100**, 153002 (2008).
15. LeBlanc, L. J. et al. Direct observation of *Zitterbewegung* in a Bose-Einstein condensate. *New J. Phys.* **15**, 073011 (2013).
16. Qu, C., Hamner, C., Gong, M., Zhang, C. & Engels, P. Observation of *Zitterbewegung* in a spin-orbit-coupled Bose-Einstein condensate. *Phys. Rev. A* **88**, 021604(R) (2013).
17. Hasan, M. et al. Wave packet dynamics in synthetic non-abelian gauge fields. *Phys. Rev. Lett.* **129**, 130402 (2022).
18. Schliemann, J., Loss, D. & Westervelt, R. M. *Zitterbewegung* of electronic wave packets in III-V zinc-blende semiconductor quantum wells. *Phys. Rev. Lett.* **94**, 206801 (2005).
19. Rusin, T. M. & Zawadzki, W. *Zitterbewegung* of nearly-free and tightly-bound electrons in semiconductors. *J. Phys. Condens. Matter* **19**, 136219 (2007a).
20. Biswas, T. & Ghosh, T. K. Wave packet dynamics and *Zitterbewegung* of heavy holes in a quantizing magnetic field. *J. Appl. Phys.* **115**, 213701 (2014).
21. Zawadzki, W. *Zitterbewegung* and its effects on electrons in semiconductors. *Phys. Rev. B* **72**, 085217 (2005).
22. Schliemann, J., Loss, D. & Westervelt, R. M. *Zitterbewegung* of electrons and holes in III-V semiconductor quantum wells. *Phys. Rev. B* **73**, 085323 (2006).
23. Schliemann, J. Cyclotron motion and magnetic focusing in semiconductor quantum wells with spin-orbit coupling. *Phys. Rev. B* **77**, 125303 (2008).
24. Rusin, T. M. & Zawadzki, W. Theory of electron *Zitterbewegung* in graphene probed by femtosecond laser pulses. *Phys. Rev. B* **80**, 045416 (2009).
25. Cserti, J. & Dávid, G. Unified description of *Zitterbewegung* for spintronic, graphene, and superconducting systems. *Phys. Rev. B* **74**, 172305 (2006).
26. Rusin, T. M. & Zawadzki, W. Transient *Zitterbewegung* of charge carriers in mono- and bilayer graphene, and carbon nanotubes. *Phys. Rev. B* **76**, 195439 (2007b).
27. Trauzettel, B., Blanter, Y. M. & Morpurgo, A. F. Photon-assisted electron transport in graphene: scattering theory analysis. *Phys. Rev. B* **75**, 035305 (2007).
28. Maksimova, G. M., Demikhovskii, V. Y. & Frolova, E. V. Wave packet dynamics in a monolayer graphene. *Phys. Rev. B* **78**, 235321 (2008).
29. Rusin, T. M. & Zawadzki, W. *Zitterbewegung* of electrons in graphene in a magnetic field. *Phys. Rev. B* **78**, 125419 (2008).
30. Deng, H., Ye, F., Malomed, B. A., Chen, X. & Panoiu, N. C. Optically and electrically tunable dirac points and *Zitterbewegung* in graphene-based photonic superlattices. *Phys. Rev. B* **91**, 201402 (2015).
31. Serna, E., Rodríguez Vargas, I., Pérez-Álvarez, R. & Diago-Cisneros, L. Pseudospin-dependent *Zitterbewegung* in monolayer graphene. *J. Appl. Phys.* **125**, 203902 (2019).
32. Lavor, I. R. et al. Effect of *Zitterbewegung* on the propagation of wave packets in ABC-stacked multilayer graphene: an analytical and computational approach. *J. Phys. Condens. Matter* **33**, 095503 (2021).
33. Wang, Y.-X., Yang, Z. & Xiong, S.-J. Study of *Zitterbewegung* in graphene bilayer with perpendicular magnetic field. *Europhys. Lett.* **89**, 17007 (2010).
34. Lavor, I. R. et al. *Zitterbewegung* of moiré excitons in twisted MoS_2/WSe_2 heterobilayers. *Phys. Rev. Lett.* **127**, 106801 (2021).
35. Zhang, X. Observing *Zitterbewegung* for photons near the Dirac point of a two-dimensional photonic crystal. *Phys. Rev. Lett.* **100**, 113903 (2008).
36. Otterbach, J., Unanyan, R. G. & Fleischhauer, M. Confining stationary light: Dirac dynamics and Klein tunneling. *Phys. Rev. Lett.* **102**, 063602 (2009).
37. Longhi, S. Photonic analog of *Zitterbewegung* in binary waveguide arrays. *Opt. Lett.* **35**, 235 (2010).
38. Chen, Y. et al. Non-abelian gauge field optics. *Nat. Commun.* **10**, 3125 (2019).
39. Dreisow, F. et al. Classical simulation of relativistic *Zitterbewegung* in photonic lattices. *Phys. Rev. Lett.* **105**, 143902 (2010).
40. Silva, T. L., Taillebois, E. R. F., Gomes, R. M., Walborn, S. P. & Avelar, A. T. Optical simulation of the free Dirac equation. *Phys. Rev. A* **99**, 022332 (2019).
41. Barends, R. et al. Superconducting quantum circuits at the surface code threshold for fault tolerance. *Nature* **508**, 500 (2014).
42. Barends, R. et al. Coherent Josephson qubit suitable for scalable quantum integrated circuits. *Phys. Rev. Lett.* **111**, 080502 (2013).
43. Song, C. et al. Continuous-variable geometric phase and its manipulation for quantum computation in a superconducting circuit. *Nat. Commun.* **8**, 1061 (2017).
44. Klein, O. Die Reflexion von Elektronen an einem Potentialsprung nach der relativistischen Dynamik von Dirac. *Zeit. Phys.* **53**, 157 (1929).
45. Dombey, N. Seventy years of the Klein paradox. *Phys. Rep.* **315**, 41 (1999).
46. Aaij, R., (LHCb Collaboration). Observation of the mass difference between neutral charm-meson eigenstates. *Phys. Rev. Lett.* **127**, 111801 (2021).
47. Zheng, R.-H. et al. Observation of a superradiant phase transition with emergent cat states. *Phys. Rev. Lett.* **131**, 113601 (2023).
48. Hofheinz, M. et al. Synthesizing arbitrary quantum states in a superconducting resonator. *Nature* **459**, 546 (2009).
49. Bermudez, A., Martin-Delgado, M. A. & Solano, E. Mesoscopic superposition states in relativistic Landau levels. *Phys. Rev. Lett.* **99**, 123602 (2007).
50. Gerritsma, R. et al. Quantum simulation of the Klein paradox with trapped ions. *Phys. Rev. Lett.* **106**, 060503 (2011).
51. Salger, T., Grossert, C., Kling, S. & Weitz, M. Klein tunneling of a quasirelativistic Bose-Einstein condensate in an optical lattice. *Phys. Rev. Lett.* **107**, 240401 (2011).
52. Kwon, H., Tan, K. C., Volkoff, T. & Jeong, H. Nonclassicality as a quantifiable resource for quantum metrology. *Phys. Rev. Lett.* **122**, 040503 (2019).

ACKNOWLEDGEMENTS

This work was supported by the National Natural Science Foundation of China (Grants No. 12274080, No. 11875108, No. 12204105, No. 11934018, No. 92065114, and No. T2121001), Innovation Program for Quantum Science and Technology (Grant No. 2021ZD0300200), the Strategic Priority Research Program of Chinese Academy of Sciences (Grant No. XDB28000000), the Key-Area Research and Development Program of Guangdong Province, China (Gran No. 2020B0303030001), Beijing Natural Science Foundation (Grant No. Z200009), the Natural Science Funds for Distinguished Young Scholar of Fujian Province under Grant 2020J06011, and Project from Fuzhou University under Grants No. JG202001-2 and No. 049050011050.

AUTHOR CONTRIBUTIONS

S.-B.Z. theoretically predicted phase space quantum interference of Dirac particles and conceived the experimental simulation. W.N. and R.-H.Z. performed numerical and experimental simulations, under the supervision of Z.-B.Y. and S.-B.Z., F.W. analyzed the data with support from R.-H.Z., S.-B.Z., Z.-B.Y., and F.W. co-wrote the paper. All authors contributed to the interpretation of observed phenomena and helped to improve the presentation of the paper.

COMPETING INTERESTS

The authors declare no competing interests.

ADDITIONAL INFORMATION

Supplementary information The online version contains supplementary material available at https://doi.org/10.1038/s41534-023-00770-0.

Correspondence and requests for materials should be addressed to Fan Wu, Zhen-Biao Yang or Shi-Biao Zheng.